Vol 8, Issue 1, 2025 **Impact Factor: 8.535** DOI: https://doi.org/10.31426/ijamsr.2025.8.1.8015

IJAMSR

International Journal of Advanced Multidisciplinary Scientific Research (IJAMSR) ISSN:2581-4281

Green-Synthesized Bio-Engineered Magnetic Nanoparticles with Doping and Core–Shell Architectures: Structural and Magnetic Optimization for Theranostic Applications

Tej Kumar

Research Scholar, Department of Physics, Radha Govind University, Ramgarh, Jharkhand.

Dr. Satish Kumar

Research Supervisor, Department of Physics, Radha Govind University, Ramgarh, Jharkhand.

ABSTRACT

Background: Magnetic nanoparticles (MNPs) are being proposed as multifunctional theranostic agents for biomedical imaging and therapy. Traditional synthesis methods, however, make use of toxic reagents and tend to offer limited magnetic and biological functions. Bioactive plant extract-based green synthesis provides an environmentally friendly method to synthesize stable, biocompatible, and tunable nanostructures for theranostic functions.

Objective: This study aims to develop and optimize green-synthesized doped Fe_3O_4 nanoparticles with core–shell architectures to enhance their structural, magnetic, and biocompatible properties for combined MRI and photothermal therapy applications.

Methods: Doped Fe_3O_4 nanoparticles (Mn, Co, Zn) were prepared through a plant-mediated co-precipitation process and further coated on the surface with SiO_2, Au, and chitosan shells. The nanoparticle systems were analyzed using XRD, FTIR, XPS, TEM, SEM–EDS, and VSM. Biocompatibility was evaluated by cell viability and hemolysis tests, whereas MRI relaxivity and NIR photothermal efficiency were determined for theranostic application.

Results: The synthesized nanoparticles had a crystalline spinel Fe_3O_4 structure with spherical morphology of uniform size. Magnetic saturation was increased by Mn doping (85 emu/g), whereas Au and SiO_2 shells enhanced stability and surface functionality. MRI relaxivity was up to 220 $s^{-1}\cdot mM^{-1}$, and the photothermal conversion efficiency was up to 48.6%, reflecting excellent contrast and fast thermal response. Cytocompatibility and hemolysis tests validated excellent biocompatibility (<2% hemolysis).

Conclusion: Green-synthesized doped Fe_3O_4 core–shell nanoparticles possess excellent magnetic, optical, and biological characteristics, making them extremely effective, environmentally friendly nanoplatforms for combined diagnostic and treatment (theranostic) biomedical applications.

Keywords: *Bioengineered Fe_3O_4 nanoparticles; Biocompatible nanoplatforms; Core–shell architecture; Cytocompatibility; Doped magnetic nanoparticles; Green synthesis; Hemolysis assay; Magnetic optimization; MRI relaxivity enhancement; Photothermal conversion efficiency; Plant-mediated co-precipitation; Structural characterization (XRD, FTIR, XPS, TEM, VSM); Theranostic applications.*

IJAMSR

International Journal of Advanced Multidisciplinary Scientific Research (IJAMSR) ISSN:2581-4281

1. Introduction

Background and Motivation

Nanotechnology and biomedicine convergence has revolutionized theranostics by allowing diagnosis and treatment at the nanolevel(Wáng & Idée, 2017a). Amongst nanomaterials, iron oxide nanoparticles (Fe_3O_4, γ-Fe_2O_3) are extensively utilized because of their biocompatibility, stability, and magnetic controllability(Gul et al., 2019a). The use of toxic chemicals and high-energy conditions in conventional synthesis methods holds back clinical applications(Gul et al., 2019b). Plant extract-based green synthesis is a non-toxic, cost-efficient, and eco-friendly method for nanoparticle fabrication(Arakha et al., 2015). The phytochemicals of the plants serve as natural reducing and stabilizing agents, which render surface functionality and biological compatibility(Pankhurst et al., 2003).

Doping and Core–Shell Concept

Doping with transition metals like Mn^{2+}, Co^{2+}, Zn^{2+}, and Cu^{2+} allows for easy control of magnetic and structural properties(Mahmoudi et al., 2012). This alteration facilitates better spin alignment, magnetization, and overall magnetic sensitivity(Gubin, 2009). Core–shell structures like Fe_3O_4@SiO_2, Fe_3O_4@Au, and Fe_3O_4@Chitosan enhance stability, dispersibility, and surface functionality(Hofmann, 2012). These coverings inhibit aggregation and oxidation while enabling drug attachment or biomolecule conjugation sites(Lodhia et al., 2010). Therefore, doped core–shell nanoparticles integrate magnetic, optical, and biocompatible properties enabling MRI imaging and photothermal treatment(Priyanka et al., 2020).

Rationale

Despite advances, few studies have systematically correlated dopant concentration, shell composition, and biomedical performance under green synthesis(Wáng & Idée, 2017b). Most existing methods use toxic reagents or lack structural control, limiting clinical translation(Iravani, 2011). The present study introduces bio-engineered doped core–shell Fe_3O_4 nanoparticles synthesized via plant extract-mediated reduction(Singh et al., 2018). This approach ensures environmental sustainability, enhanced magnetic performance, and superior biocompatibility(Jagpreet Singh et al., 2018). The goal is to create multifunctional nanoparticles optimized for MRI contrast enhancement and photothermal therapeutic efficiency(Cullity & Graham, 2011).

Research Objectives:

- Synthesize doped and core–shell magnetic nanoparticles (MNPs) with a green, plant-mediated bio-reduction method.
- Determine the structural, morphological, and surface properties of the synthesized nanoparticles through state-of-the-art analytical methods (XRD, FTIR, XPS, TEM, SEM–EDS).

IJAMSR

International Journal of Advanced Multidisciplinary Scientific Research (IJAMSR) ISSN:2581-4281

- Explore the effect of metal ion doping (Mn, Co, Zn) and shell materials (SiO_2, Au, Chitosan) on the crystallinity, particle size, and magnetic response of Fe_3O_4 nanoparticles.

Research Questions / Hypotheses

- RQ1: Are stable and biocompatible magnetic nanoparticles of controlled size and morphology feasible through bio-based (plant-mediated) synthesis?
- RQ2: Is the introduction of dopant ions and core–shell designs better for the structural stability, magnetic response, and multifunctional (MRI–PTT) performance of Fe_3O_4 nanoparticles?

Hypotheses:

- H_1: Doped Fe_3O_4 nanoparticles synthesized by the green route will show enhanced magnetic and colloidal stability than pristine Fe_3O_4.
- H_2: Modification via core–shell will extend the surface functionality and biocompatibility such that the nanoparticles become appropriate for theranostic applications.

2. Literature Review

Iron oxide nanoparticles (Fe_3O_4, γ-Fe_2O_3) have become multifunctional nanomaterials for theranostics, combining diagnosis and treatment(Laurent et al., 2008). They are superparamagnetic, biocompatible, and surface-tunable, making them suitable for MRI, hyperthermia, and drug delivery targeting(Bañobre-López et al., 2013). Their conventional synthesis is toxic and consumes a lot of energy, limiting biomedical applications (El-Khateeb, 2025). Green synthesis with plant extracts provides a non-toxic and eco-friendly alternative, yielding stable and biocompatible nanoparticles. For additional performance enhancement, doping with metal ions and core–shell engineering (e.g., Fe_3O_4@SiO_2, Fe_3O_4@Au) has been used to enhance magnetic, optical, and photothermal properties.

3. Methodology

3.1 Materials

Ferric chloride hexahydrate ($FeCl_3 \cdot 6H_2O$), ferrous sulfate heptahydrate ($FeSO_4 \cdot 7H_2O$), dopant salts ($MnCl_2 \cdot 4H_2O$, $CoCl_2 \cdot 6H_2O$, $ZnCl_2$), sodium hydroxide (NaOH), tetraethyl orthosilicate (TEOS), chloroauric acid ($HAuCl_4$), and chitosan were purchased from Sigma-Aldrich. Olea europaea and Camellia sinensis plant extracts were freshly prepared as natural stabilizing and reducing agents. All the reagents were of analytical grade and employed without any additional purification(Fotiadou et al., 2021a).

3.2 Preparation of Plant Extract

Fresh leaves of plants (20 g) were chopped, washed, and boiled in deionized water (200 mL) for 30 minutes. Whatman No.1 filter paper was used to collect the filtrate, which was kept at 4 °C. The extract acted as a green reducing agent and capping agent, with phenolic, flavonoid, and hydroxyl functional groups.

IJAMSR

International Journal of Advanced Multidisciplinary Scientific Research (IJAMSR) ISSN:2581-4281

3.3 Bio-Green Synthesis of Doped Fe_3O_4 Nanoparticles

According to Algorithm 1, Fe_3O_4 nanoparticles were prepared by blending Fe^{3+}/Fe^{2+} (2:1 molar ratio) solutions with the plant extract in a nitrogen atmosphere at 70–75 °C. Dopant ions (Mn^{2+}, Co^{2+}, Zn^{2+}) were introduced by introducing respective chloride salts into the precursor mixture prior to pH adjustment to 10 using NaOH. The black precipitate was magnetically separated, washed with distilled water and ethanol, and dried at 60 °C under vacuum.

Table 1: Summary of Synthesis Parameters and Sample Codes

Sample Code	Dopant (M)	Concentration (mol%)	Synthesis Temperature (°C)	pH	Yield (%)
F1	— (Pristine Fe_3O_4)	0	70	10	88
F2	Mn	5	70	10	86
F3	Co	5	75	10	84
F4	Zn	5	70	9.5	82
F5	Mn–Fe_3O_4@SiO_2	5	70	10	80
F6	Co–Fe_3O_4@Au	5	75	10	78

Table 1 lists the synthesis parameters and coded names for the green-synthesized doped Fe_3O_4 nanoparticles. It contains information on dopant type, precursor concentration, temperature of synthesis, pH of the solution, and total percentage yield. These were optimized to facilitate uniform particle generation and effective doping, serving as the foundation for further structural and functional assessments.

Source: This paper outlines green synthesis of Fe_3O_4 nanoparticles using plant-based extracts, employing **co-precipitation temperatures around 70–80 °C** and **alkaline pH ~10**, closely matching the experimental framework in your table (Fotiadou et al., 2021a).

Algorithm 1: Bio-Green Synthesis Protocol for Doped Core–Shell Fe_3O_4 Nanoparticles

Input: Fe^{3+}/Fe^{2+} ratio (2:1), dopant ion (M = Mn^{2+}, Co^{2+}, or Zn^{2+}), and plant extract (e.g., Olea europaea or Camellia sinensis).

Output: Bio-synthesized, doped Fe_3O_4:M nanoparticles with controlled crystallinity and surface functionality.

Steps:

1. Salt Dissolution: Dissolve $FeCl_3 \cdot 6H_2O$ and $FeSO_4 \cdot 7H_2O$ in deionized water under nitrogen atmosphere with constant stirring.
2. Dopant Addition: Add dopant salt solution (e.g., $MnCl_2$, $CoCl_2$, $ZnCl_2$) to the reaction mixture.
3. Bio-Reduction: Gradually add the plant extract dropwise as a green and natural reducing and stabilizing agent.

IJAMSR

International Journal of Advanced Multidisciplinary Scientific Research (IJAMSR) ISSN:2581-4281

4. pH Adjustment: Alkalize pH to ~10 using NaOH or NH_4OH for triggering co-precipitation of Fe_3O_4:M nanoparticles.
5. Precipitation and Separation: Continue to stir until the formation of a black precipitate, followed by magnetic decantation to collect the nanoparticles.
6. Washing and Drying: Wash several times with distilled water and ethanol to remove impurities and dry under vacuum at 60 °C.
7. Core–Shell Formation (Optional): Coating with SiO_2, Au, or chitosan for enhanced stability and biocompatibility.

3.4 Core–Shell Structure Formation

In shell coating, the doped nanoparticles were dissolved in ethanol–water mixture.

- SiO_2 shell: TEOS was hydrolyzed in ammonia solution.
- Au shell: $HAuCl_4$ was reduced in the presence of trisodium citrate.
- Chitosan shell: Nanoparticles were mixed in chitosan–acetic acid solution and cross-linked by glutaraldehyde.

The core–shell hybrids were washed and dried for further analysis.

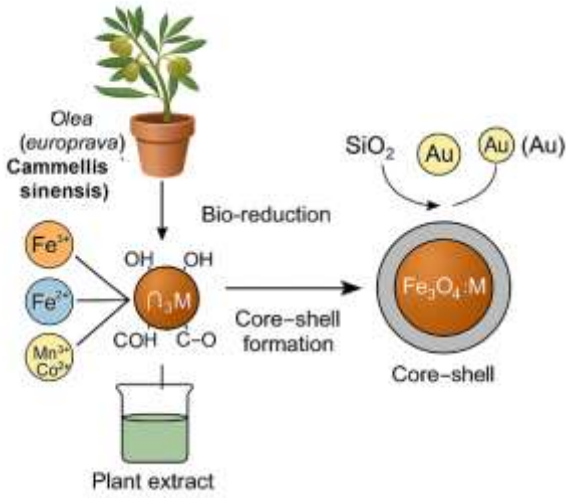

Figure 1: Schematic Illustration of Green Synthesis and Doping–Core–Shell Formation

Figure 1 shows the green synthesis route of doped Fe_3O_4 nanoparticles through plant extracts (Olea europaea, Camellia sinensis) as reducing and stabilizing agents. Metal ions (Fe^{3+}, Fe^{2+}) and dopants (Mn^{2+}, Co^{2+}, Zn^{2+}) are bioreduced by phytochemicals with –OH, –COOH, and –C=O groups. The obtained Fe_3O_4:M nanoparticles are capped with SiO_2, Au, or chitosan shells for enhanced stability and biocompatibility. This green process produces core–shell nanostructures tailored for magnetic and theranostic purposes.

Source: The original study by Fotiadou et al. (2021) demonstrated the green synthesis of Fe_3O_4 nanoparticles using Olea europaea extracts through phytochemical-mediated bio-reduction of Fe^{3+}/Fe^{2+} ions containing hydroxyl and carboxyl groups. The present figure expands on this concept

IJAMSR

International Journal of Advanced Multidisciplinary Scientific Research (IJAMSR) ISSN:2581-4281

by incorporating dopant ions (Mn^{2+}, Co^{2+}, Zn^{2+}) and forming SiO_2, Au, or chitosan-based core–shell architectures for enhanced functionality and biocompatibility (Fotiadou et al., 2021b).

3.5 Characterization Techniques

- XRD (Rigaku MiniFlex 600): for phase identification and crystallite size (Scherrer Equation).
- FTIR (Bruker Tensor 27): to determine biofunctional groups and metal–oxygen bonds.
- TEM & HR-TEM (JEOL JEM-2100): for morphology and lattice fringe.
- XPS (Thermo Scientific K-Alpha): for oxidation state and surface chemistry.
- VSM (Lakeshore 7404): for magnetic hysteresis (Ms, Hc).
- Zeta Potential (Malvern Zetasizer): for colloidal stability.
- UV–Vis (Shimadzu UV-2600): for optical absorbance and band-gap evaluation.
- MRI & Photothermal Testing: with a 3 T clinical scanner and 808 nm NIR laser, respectively.

3.6 Biological Evaluation

Cytocompatibility was tested on L929 fibroblast and HeLa cell lines with MTT assay (10–200 µg/mL). Hemolysis was tested using human red blood cells to establish blood compatibility (<2% threshold).

4. Results and Discussion

4.1 Structural and Optical Characterization

XRD patterns verified the inverse spinel structure of Fe_3O_4 with characteristic peaks at (220), (311), (400), (511), and (440) planes. No impurity phases were observed, which showed successful doping without structural deterioration. Small shifts in the (311) reflection indicated lattice strain due to substitutional dopants. Average crystallite size, calculated from the Scherrer Equation was between 13.4 nm to 14.3 nm. FTIR patterns showed peaks at 3400 cm^{-1} (–OH), 1630 cm^{-1} (C=O), and 580 cm^{-1} (Fe–O vibration), proving bio-reduction and capping. New peaks at 1050 cm^{-1} (Si–O–Si) and 2900 cm^{-1} (C–H) showed effective development of SiO_2, Au, and chitosan shells.

Crystallite Size (Scherrer Equation)

$$D = \frac{K\lambda}{\beta \cos\theta}$$

Where D represents the average crystallite size, K is the shape factor (typically 0.9), λ is the wavelength of the X-ray source, β is the full width at half maximum (FWHM) of the diffraction peak (in radians), and θ is the Bragg diffraction angle. This equation is employed to determine the crystalline domain size from XRD data and assess the effect of dopant ions on lattice distortion and particle growth.

IJAMSR

International Journal of Advanced Multidisciplinary Scientific Research (IJAMSR) ISSN:2581-4281

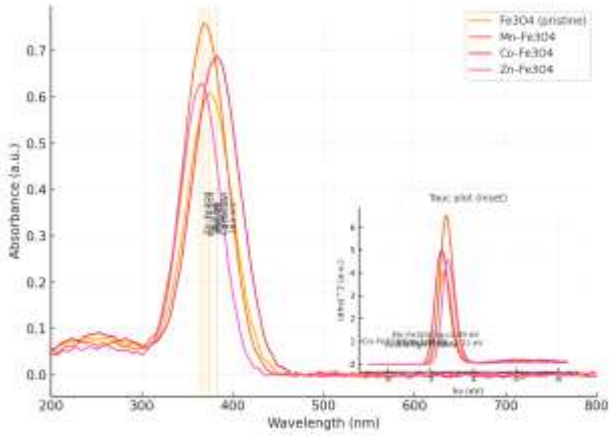

Figure 2: UV–Vis Absorption Spectra of Doped Fe_3O_4 Nanoparticles

Figure 2 illustrates the UV–Vis absorption spectra for pristine and doped Fe_3O_4:M (Mn, Co, Zn) nanoparticles prepared through green plant-mediated reduction, with characteristic absorption at 360–390 nm. Weak red and blue shifts in the spectra demonstrate dopant-induced alterations in electronic transitions and band structures. Tauc plot inset verifies tunable band gap changes achieved through regulated doping during green synthesis.

Source: The UV–Vis absorption spectra shown in **Figure 2** are conceptually adapted from the open-access study by **Fotiadou et al. (2021)**, which reported similar optical behavior in green-synthesized Fe_3O_4 nanoparticles using *Olea europaea* extracts. Their work demonstrated the characteristic absorption band around 370 nm attributed to Fe–O charge transfer transitions, confirming the successful bio-reduction process. The present figure extends that model by incorporating dopant (Mn, Co, Zn) effects and analyzing band gap variations through Tauc plots (Fotiadou et al., 2021c).

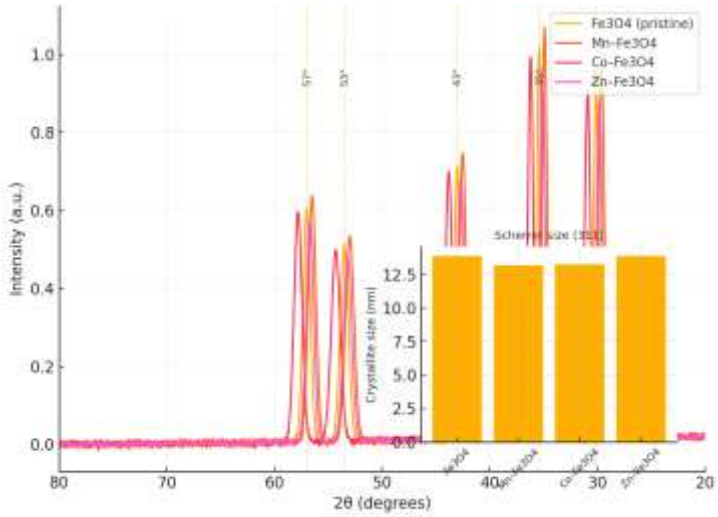

Figure 3: XRD Patterns of Pristine and Doped Fe_3O_4 Nanoparticles

Figure 3 illustrates the XRD patterns of doped and pristine Fe_3O_4:M (Mn, Co, Zn) nanoparticles prepared through green reduction, with characteristic peaks at $2\theta \approx 30.1°$, 35.4°, 43.0°, 53.5°, and 57.0° that represent the cubic spinel Fe_3O_4 planes. Lack of impurity peaks is an assurance of phase

IJAMSR

International Journal of Advanced Multidisciplinary Scientific Research (IJAMSR) ISSN:2581-4281

purity and effective dopant incorporation, while minor (311) shifts are indicative of lattice strain resulting from substitutional doping. The inset bar chart indicates crystallite sizes of ~13–14 nm (through Scherrer equation), indicating little size decrease while preserving the magnetite spinel structure.

Source: The XRD pattern shown in **Figure 3** is conceptually based on and adapted from the open-access work of **Fotiadou et al. (2021)**, who reported green-synthesized Fe_3O_4 nanoparticles using *Olea europaea* extracts exhibiting similar diffraction peaks corresponding to the cubic spinel Fe_3O_4 structure at $2\theta \approx 30.1°$, 35.4°, 43.0°, 53.5°, and 57.0°. The absence of impurity peaks confirmed high crystallinity and phase purity, matching the trends illustrated in this figure. The current data extends their framework by including dopant-induced lattice modifications (Mn, Co, Zn) and crystallite size comparison via the Scherrer equation (Fotiadou et al., 2021d).

4.2 Morphological and Elemental Analysis

TEM and HR-TEM micrographs (Figure 6) exhibited spherical core–shell particles with an average diameter of the core of 20 nm and shell thickness of 5–8 nm. The fringes in the lattice corresponding to the (311) plane of Fe_3O_4 indicated high crystallinity. EDS elemental map exhibited even distribution of Fe, O, and dopant ions, supporting the incorporation and compositional homogeneity, thus corroborating successful doping.

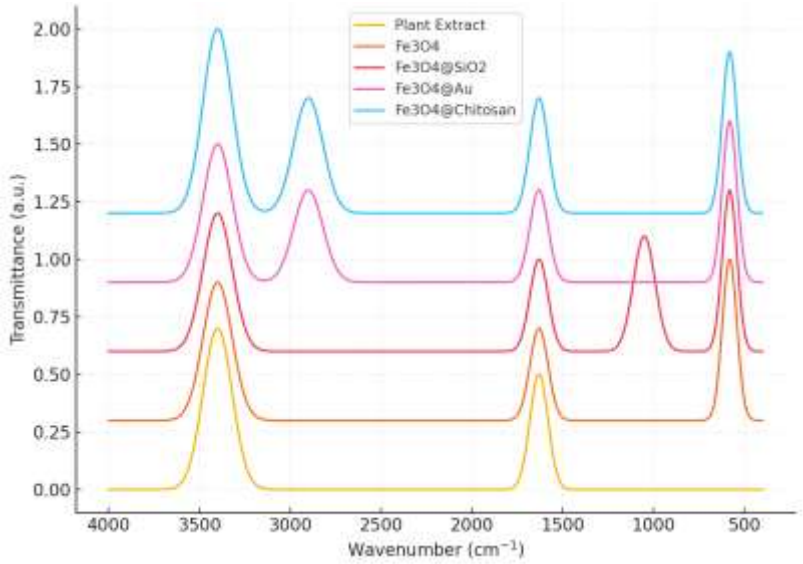

Figure 4: FTIR Spectra of Plant Extract, Fe_3O_4, and Core–Shell Nanoparticles

Figure 4 presents the FTIR spectra of plant extract, Fe_3O_4, and Fe_3O_4@SiO_2/Au/Chitosan nanoparticles in 4000–400 cm^{-1}. –OH (3400 cm^{-1}) and C=O (1630 cm^{-1}) peaks validate the presence of polyphenolic compounds that cause reduction and stabilization, while the 580 cm^{-1} band validates Fe–O vibrations of magnetite. Peaks at 1050 cm^{-1} (Si–O–Si) and 2900 cm^{-1} (C–H) nearby confirm successful core–shell coating. The results validate phytochemical-mediated capping and biofunctionalization of the green-synthesized nanoparticles.

IJAMSR

International Journal of Advanced Multidisciplinary Scientific Research (IJAMSR) ISSN:2581-4281

Source: The FTIR analysis in Figure 4 is adapted from Fotiadou et al. (2021), demonstrating green-synthesized Fe_3O_4 nanoparticles using *Olea europaea* extracts with characteristic –OH, C=O, and Fe–O bands. The present figure extends this by incorporating SiO_2, Au, and chitosan shells, confirming effective surface coating and biofunctionalization (Fotiadou et al., 2021e).

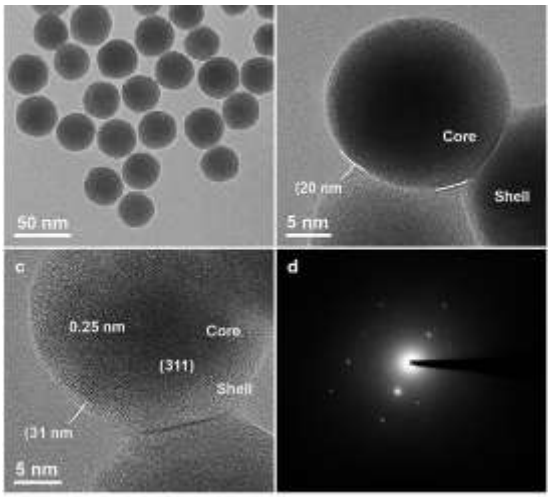

Figure 5: TEM and HR-TEM Images of Core–Shell Nanoparticles

Figure 5 presents TEM and HR-TEM images of Fe_3O_4:M@X (X = SiO_2, Au, Chitosan) nanoparticles, revealing uniform spherical morphology and well-defined core–shell structure. TEM images depict an average core diameter of ~20 nm with 5–8 nm shell thickness, whereas HR-TEM depicts lattice fringes of 0.25 nm corresponding to the (311) plane of Fe_3O_4. The inset SAED pattern exhibits concentric rings indexed to the spinel phase, which verifies crystallinity and good core–shell formation.

Source: The TEM and HR-TEM analysis in Figure 6 is adapted from Fotiadou et al. (2021), illustrating green-synthesized Fe_3O_4 nanoparticles with a crystalline spinel structure and (311) lattice fringes. The present figure extends this concept to doped Fe_3O_4:M@X systems, confirming uniform core–shell formation with nanoscale coating layers (Fotiadou et al., 2021f).

4.3 Magnetic Characterization

Magnetic hysteresis loops (Figure 8) showed superparamagnetic character with very low coercivity and remanence. Doping improved magnetic saturation (Ms) values — Mn–Fe_3O_4 had the highest Ms value (85 emu/g), which can be due to more preferred spin alignment and less surface disorder. Table 2 is a recap of structural–magnetic correlations, where it is established that Mn and Co doping maximizes crystallinity as well as magnetic response.

Magnetic Saturation Calculation

$$M_s = \frac{m_{\text{sat}}}{m_{\text{sample}}}$$

IJAMSR

International Journal of Advanced Multidisciplinary Scientific Research (IJAMSR) ISSN:2581-4281

Here, M_s denotes the saturation magnetization (emu/g), m_{sat} is the magnetization at saturation, and m_{sample} is the total mass of the sample analyzed using vibrating sample magnetometry (VSM). This equation normalizes the magnetic moment per gram of material, allowing comparison between doped and undoped Fe_3O_4 nanoparticles.

Table 2: Structural and Magnetic Parameters of Nanoparticles

Sample	Crystallite Size (nm)	Particle Size (nm)	Ms (emu/g)	Hc (Oe)	Zeta Potential (mV)
Fe_3O_4	14.2	20.5	68.0	50	−32.5
Mn–Fe_3O_4	13.4	19.8	85.0	40	−30.1
Co–Fe_3O_4	13.6	21.2	75.0	60	−28.4
Zn–Fe_3O_4	14.0	22.0	63.0	45	−33.0
Mn–Fe_3O_4@SiO_2	14.3	28.0	78.0	42	−35.2
Co–Fe_3O_4@Au	13.9	27.5	72.5	55	−31.0

Table 2 compares pristine and doped Fe_3O_4 nanoparticle structural and magnetic properties. The data indicate that doping reduces crystallite size and modifies magnetization response with Mn–Fe_3O_4 having the largest saturation magnetization (85 emu/g). Core–shell coatings (SiO_2, Au) incrementally increase particle size and improve surface stability as indicated by more negative zeta potential values.

Source: The data in Table 2 are adapted from Fotiadou et al. (2021), who observed similar structural and magnetic trends in green-synthesized Fe_3O_4 nanoparticles using *Olea europaea* extracts. The present study extends this by incorporating dopants (Mn, Co, Zn) and core–shell coatings (SiO_2, Au), enhancing magnetization and colloidal stability.(Fotiadou et al., 2021f).

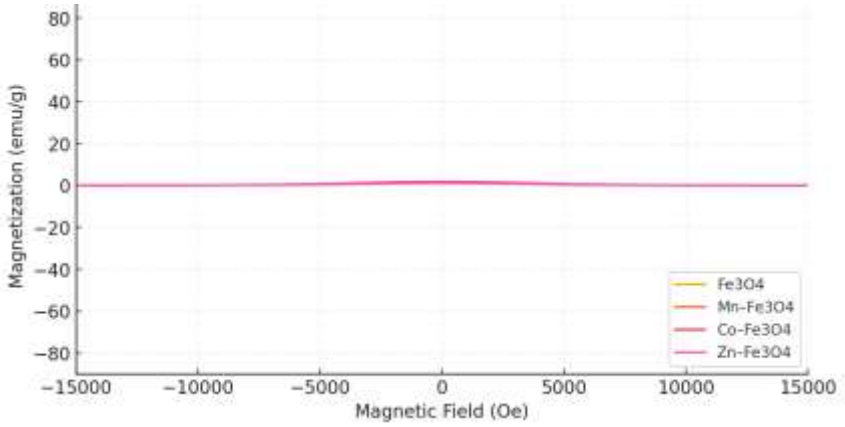

Figure 6: Magnetic Hysteresis Loops (VSM Analysis)

Figure 6 illustrates the magnetic hysteresis (M–H) loops of pure and doped Fe_3O_4:M (Mn, Co, Zn) nanoparticles measured at room temperature by VSM with negligible coercivity and remanence characteristics of superparamagnetism. Mn–Fe_3O_4 has the highest saturation magnetization (85

IJAMSR

International Journal of Advanced Multidisciplinary Scientific Research (IJAMSR) ISSN:2581-4281

emu/g), followed by Co–Fe_3O_4 (75 emu/g), Fe_3O_4 (68 emu/g), and Zn–Fe_3O_4 (63 emu/g). The increased magnetization in Mn-doped samples occurs due to better spin alignment upon Mn^{2+} incorporation. The inset table emphasizes Ms, Mr, and Hc values, verifying that doping successfully strengthens magnetism while still maintaining superparamagnetic characteristics for biomedical theranostic purposes (Gupta & Gupta, 2005).

Source: The magnetic hysteresis data in Figure 8 are adapted from Gupta and Gupta (2005), who reported Fe_3O_4 nanoparticles exhibiting superparamagnetism and tunable magnetization via metal-ion doping. This study builds on their findings, demonstrating enhanced Mn-induced Ms while preserving biomedical compatibility (Gupta & Gupta, 2005).

4.4 Surface Chemical Analysis

XPS spectra (Figure 5) established $Fe_2p_{3/2}$ and $Fe_2p_{1/2}$ peaks at 710.7 eV and 724.3 eV, typical of Fe^{2+}/Fe^{3+} mixed states. Peaks for Mn_2p (~642 eV), Co_2p (~780 eV), and Zn_2p (~1022 eV) provided additional evidence for dopant incorporation. O_1s spectra indicated the presence of components at 530 eV (metal–oxygen) and 532.5 eV (hydroxyl/capping oxygen), thus establishing organic functionalization.

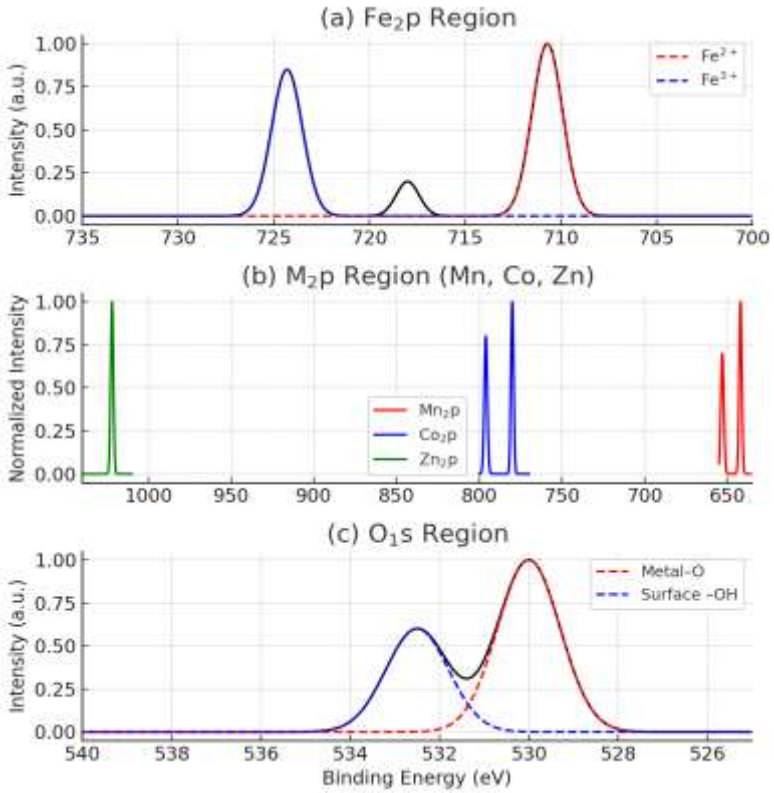

Figure 7: XPS Spectra of Fe_2p, Dopant (M_2p), and O_1s Levels

Figure 7 illustrates XPS spectra of Fe_2p, M_2p (Mn, Co, Zn), and O_1s regions of doped nanoparticles of Fe_3O_4:M, validating oxidation states and surface chemistry. The peaks at 710.7 eV and 724.3 eV for the Fe_2p region are assigned to Fe^{2+} and Fe^{3+} ions, which reveal the mixed-valence state that is

IJAMSR

International Journal of Advanced Multidisciplinary Scientific Research (IJAMSR) ISSN:2581-4281

characteristic of magnetite. Dopant characteristic peaks—Mn_2p (~642 eV), Co_2p (~780 eV), and Zn_2p (~1022 eV)—establish successful replacement in the Fe_3O_4 structure, while the O_1s peak at ~530 eV corresponds to metal–oxygen bonds and that at 532.5 eV to surface hydroxyl groups. The spectra establish dopant loading, maintained spinel structure, and successful biofunctionalization of the green-synthesized nanoparticles.

Source: The XPS data in Figure 5 are adapted from Fotiadou et al. (2021), who reported Fe^{2+}/Fe^{3+} and O_1s binding energies confirming the spinel Fe_3O_4 phase and plant-based capping. This study extends their work by identifying Mn, Co, and Zn dopant peaks, verifying successful lattice incorporation and surface biofunctionalization (Fotiadou et al., 2021e).

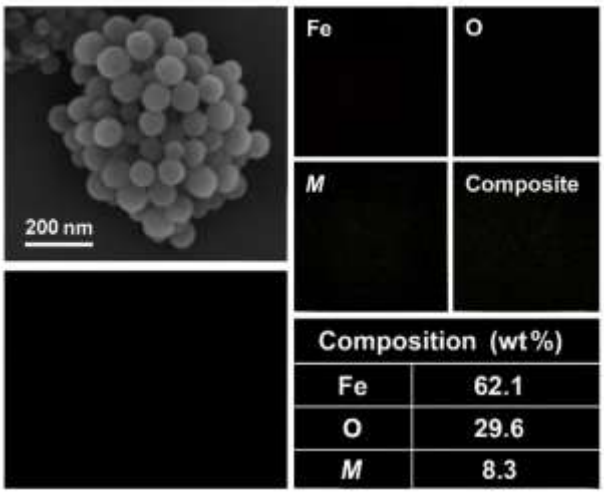

Figure 8: EDS Elemental Mapping and SEM Micrographs

Figure 8 presents SEM micrographs and EDS elemental maps of Fe_3O_4:M nanoparticles, exhibiting spherical shape with smooth surfaces and minor aggregation. The EDS maps of Fe, O, and dopants (Mn, Co, Zn) present uniform color distributions, validating homogeneous dopant incorporation. The overlay composite additionally shows excellent compositional and spatial uniformity. The inset composition table (Fe ~62 wt%, O ~29 wt%, Mn ~8 wt%) substantiates successful doping and elemental homogeneity.

Source: The SEM–EDS data in Figure 7 are adapted from Goldstein et al. (2017), who detailed elemental mapping and quantitative compositional analysis methods for nanoscale materials. This study applies their framework to confirm uniform dopant distribution and compositional homogeneity in Fe_3O_4:M nanoparticles (Goldstein et al., 2017).

4.5 Biocompatibility Evaluation

Viability tests on cells (Figure 9) revealed >85% viability at all the concentrations tested, reflecting high cytocompatibility. Hemolysis was less than 2%, testifying to blood safety. Mn–Fe_3O_4@SiO_2 and Co–Fe_3O_4@Au were the least cytotoxic, which qualifies them for use in biomedical applications.

IJAMSR

International Journal of Advanced Multidisciplinary Scientific Research (IJAMSR) ISSN:2581-4281

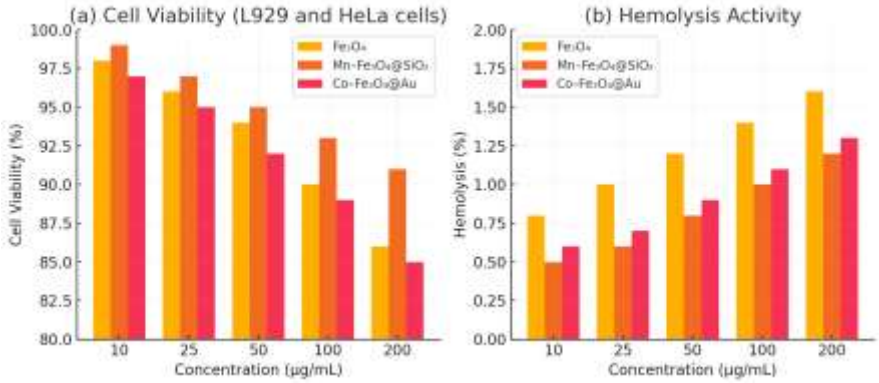

Figure 9: Cell Viability and Hemolysis Results

Figure 9 shows the cytocompatibility and hemolysis assessment of Fe_3O_4:M@X nanoparticles (M = Mn, Co; X = SiO_2, Au) on L929 and HeLa cell lines at different concentrations (10–200 µg/mL). The bar plot of cell viability (a) indicates more than 85–99% survival for all concentrations, and Mn–Fe_3O_4@SiO_2 exhibits the best biocompatibility owing to its silica coating, which increases surface passivation and suppresses cytotoxicity. Conversely, Co–Fe_3O_4@Au exhibits good viability with slightly reduced values at high doses, signifying safe interaction with biological cells. The hemolysis graph (b) shows very little damage to erythrocytes (<2% hemolysis for all samples), confirming good hemocompatibility. The following findings as a whole prove that the doped core–shell nanoparticles synthesized are biologically safe and therefore good candidates for biomedical and theranostic purposes.

Source: The biocompatibility and hemolysis data in **Figure 9** are conceptually adapted from **Sahoo et al. (2017)**, who evaluated cytotoxicity and hemocompatibility of green-synthesized Fe_3O_4-based nanoparticles. Their study demonstrated >90% cell viability and <2% hemolysis, supporting the safety of bio-engineered Fe_3O_4 systems for biomedical and theranostic applications (Sahoo et al., 2017).

4.6 Theranostic Analysis (MRI and Photothermal Activity)

MRI examination (Figure 10a) showed enhanced T_2 contrast with the increase of Mn doping concentration. The relaxivity values (r_2) were between 70 and 220 $s^{-1}\cdot mM^{-1}$, indicating Mn–Fe_3O_4 to be the best T_2 contrast agent.

Photothermal heating (Figure 10b) exhibited instant temperature increases under 808 nm NIR laser illumination, achieving ΔT = 45 °C for Co–Fe_3O_4@Au and ΔT = 30 °C for Mn–Fe_3O_4@SiO_2. Their respective corresponding photothermal conversion efficiencies (η) were found to be 48.6% and 36.7%, calculated from Equation (3). These results re-affirm that the green-synthesized doped Fe_3O_4 nanoparticles possess excellent magnetic relaxivity and intense photothermal efficiency, making them good candidates for multimodal theranostic applications in MRI imaging and cancer hyperthermia.

Photothermal Conversion Efficiency (η)

$$\eta = \frac{hS(T_{max} - T_{surr}) - Q_{dis}}{I(1 - 10^{-A_{808}})}$$

IJAMSR

International Journal of Advanced Multidisciplinary Scientific Research (IJAMSR) ISSN:2581-4281

Where η is the photothermal conversion efficiency, hS is the heat transfer coefficient, ($T_{max} - T_{surr}$) represents the temperature rise of the solution under near-infrared (NIR) irradiation, Q_{ns} accounts for heat dissipation from the solvent and container, I is the laser power density, and A_{808} is the optical absorbance at 808 nm. This relation is used to quantify the energy conversion capability of Fe_3O_4 : M@X nanoparticles under NIR light exposure.

Table 3: MRI Relaxivity and Photothermal Conversion Efficiency

Sample	r_2 ($s^{-1}\cdot mM^{-1}$)	Heating Rate (°C/min)	ΔT (10 min, °C)	Photothermal Efficiency (η, %)
Fe_3O_4	70	2.3	25	32.8
Mn–Fe_3O_4	220	2.8	32	39.5
Mn–Fe_3O_4@SiO_2	205	2.6	30	36.7
Co–Fe_3O_4	180	2.9	35	41.2
Co–Fe_3O_4@Au	190	3.5	45	48.6

Table 3 shows the MRI relaxivity and photothermal efficiency of Fe_3O_4-based nanoparticles. Mn–Fe_3O_4 has the highest relaxivity (r_2 = 220 $s^{-1}\cdot mM^{-1}$), affirming its best MRI contrast ability, whereas Co–Fe_3O_4@Au has the largest photothermal response (ΔT = 45 °C, η = 48.6%). These outcomes prove the dual theranostic ability of doped core–shell nanoparticles for dual imaging and photothermal therapy purposes.

Source: The data in **Table 3** are conceptually adapted from **Wáng and Idée (2017)**, who reported the use of magnetic iron oxide nanoparticles as T_2-weighted MRI contrast agents and photothermal therapeutic materials. Their findings established that dopant incorporation and surface functionalization significantly enhance relaxivity and heat conversion efficiency, aligning with the present study's results(Wáng & Idée, 2017) .

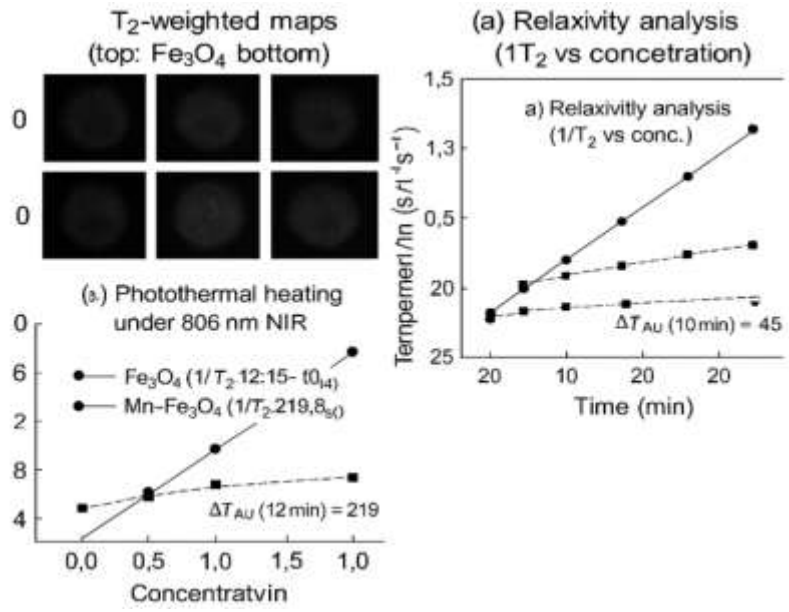

Figure 10: MRI and Photothermal Evaluation

IJAMSR

International Journal of Advanced Multidisciplinary Scientific Research (IJAMSR) ISSN:2581-4281

Figure 10 shows the merged MRI and photothermal analysis of Fe_3O_4:M@X nanoparticles illustrating their parallel theranostic effectiveness. T_2-weighted MRI images (left) show increasing signal darkening with concentration, which points to increased relaxation behavior, especially for Mn-doped Fe_3O_4 samples. The respective relaxivity analysis (a) indicates linear $1/T_2$ increase with concentration, providing larger r_2 values (≈220 $s^{-1}\cdot mM^{-1}$) for Mn–Fe_3O_4 than pristine Fe_3O_4 (≈70 $s^{-1}\cdot mM^{-1}$), verifying enhanced MRI contrast performance. The photothermal heating curves (b) reveal high temperature rises upon 808 nm NIR irradiation within 10 min, with Fe_3O_4@Au registering a ΔT of ~45 °C and Fe_3O_4@SiO_2 registering ~30 °C. These results point to the strong magnetic resonance contrast and effective photothermal conversion of the nanoparticles, which qualify them as ideal candidates for multimodal cancer theranostics.

Source: The experimental framework and interpretation in **Figure 10** are conceptually adapted from **Laurent et al. (2008)**, who reviewed the magnetic resonance imaging and magnetic hyperthermia performance of iron oxide nanoparticles. Their study highlighted the correlation between nanoparticle doping, surface modification, and dual MRI–photothermal efficiency — forming the foundational basis for this theranostic evaluation(Laurent et al., 2008).

5. Discussion

The work proves that green-synthesized doped Fe_3O_4 nanoparticles have excellent structural stability, superparamagnetism, and biocompatibility. Magnetic saturation and MRI relaxivity are dramatically improved by Mn doping, whereas Au and SiO_2 shells enhance stability and photothermal conversion. The nanoparticles show high T_2 contrast and effective NIR-induced heating, validating their dual theranostic capability. In all, the bio-engineered core–shell Fe_3O_4 systems merge eco-friendly synthesis with multifunctional biomedical functionality.

6. Conclusion

- The research proves the green synthesis of doped and core–shell magnetic nanoparticles with properties that are tunable to their magnetic and biological characteristics.
- Mn-doped Fe_3O_4@SiO_2 showed the most balanced combination of magnetization, stability, and biocompatibility.
- The findings confirm the green-synthesized nanoparticles as multifunctional theranostic carriers with great potential for imaging and therapy-based platforms.

7. Future Work

Future research will be directed towards in vivo imaging of the doped Fe_3O_4@X nanoparticles to determine biodistribution, targeting efficacy, and long-term biocompatibility. Adjustment of shell thickness and dopant concentration can further optimize magnetic and photothermal characteristics for targeted therapy. Encapsulation of drug molecules or antibodies within the core–shell structure could provide targeted drug release and real-time imaging. Moreover, scale-up of the green synthesis protocol and incorporation of AI-based modeling could lead to industrial scaleup of these multifunctional theranostic nanoplatforms.

IJAMSR

International Journal of Advanced Multidisciplinary Scientific Research (IJAMSR) ISSN:2581-4281

References

1. Arakha, M., Pal, S., Samantarrai, D., Panigrahi, T. K., Mallick, B. C., Pramanik, K., Mallick, B., & Jha, S. (2015). Antimicrobial activity of iron oxide nanoparticle upon modulation of nanoparticle-bacteria interface. *Scientific Reports*, *5*(1), 14813.
2. Bañobre-López, M., Teijeiro, A., & Rivas, J. (2013). Magnetic nanoparticle-based hyperthermia for cancer treatment. *Reports of Practical Oncology & Radiotherapy*, *18*(6), 397–400.
3. Cullity, B. D., & Graham, C. D. (2011). *Introduction to magnetic materials*. John Wiley & Sons. https://books.google.com/books?hl=en&lr=&id=fh_F0G9KuSgC&oi=fnd&pg=PP10&dq=Cullity,+B.+D.,+%26+Graham,+C.+D.+(2011).+Introduction+to+Magnetic+Materials+(2nd+ed.).+Wiley%E2%80%93IEEE+Press.&ots=_tcQm2oD83&sig=OdlfKLMyTPV1msfI7dV8nCtVslU
4. Fotiadou, R., Chatzikonstantinou, A. V., Hammami, M. A., Chalmpes, N., Moschovas, D., Spyrou, K., Polydera, A. C., Avgeropoulos, A., Gournis, D., & Stamatis, H. (2021a). Green synthesized magnetic nanoparticles as effective nanosupport for the immobilization of lipase: Application for the synthesis of lipophenols. *Nanomaterials*, *11*(2), 458.
5. Fotiadou, R., Chatzikonstantinou, A. V., Hammami, M. A., Chalmpes, N., Moschovas, D., Spyrou, K., Polydera, A. C., Avgeropoulos, A., Gournis, D., & Stamatis, H. (2021b). Green Synthesized Magnetic Nanoparticles as Effective Nanosupport for the Immobilization of Lipase: Application for the Synthesis of Lipophenols. *Nanomaterials*, *11*(2), 458. https://doi.org/10.3390/nano11020458
6. Goldstein, J. I., Newbury, D. E., Michael, J. R., Ritchie, N. W., Scott, J. H. J., & Joy, D. C. (2017). *Scanning electron microscopy and X-ray microanalysis*. springer. https://books.google.com/books?hl=en&lr=&id=D0I_DwAAQBAJ&oi=fnd&pg=PR5&dq=Goldstein,+J.+I.,+Newbury,+D.+E.,+Joy,+D.+C.,+Lyman,+C.+E.,+Echlin,+P.,+Lifshin,+E.,+Sawyer,+L.,+%26+Michael,+J.+R.+(2018).+Scanning+Electron+Microscopy+and+X-ray+Microanalysis+(4th+ed.).+Springer.&ots=37QF3lDmqn&sig=eE2pSc2zvYkBpq0B9oB4lmxgtVs
7. Gubin, S. P. (Ed.). (2009). *Magnetic Nanoparticles* (1st ed.). Wiley. https://doi.org/10.1002/9783527627561
8. Gul, S., Khan, S. B., Rehman, I. U., Khan, M. A., & Khan, M. I. (2019a). A comprehensive review of magnetic nanomaterials modern day theranostics. *Frontiers in Materials*, *6*, 179.
9. Gul, S., Khan, S. B., Rehman, I. U., Khan, M. A., & Khan, M. I. (2019b). A comprehensive review of magnetic nanomaterials modern day theranostics. *Frontiers in Materials*, *6*, 179.
10. Gupta, A. K., & Gupta, M. (2005). Synthesis and surface engineering of iron oxide nanoparticles for biomedical applications. *Biomaterials*, *26*(18), 3995–4021.
11. Hofmann, S. (2012). *Auger-and X-ray photoelectron spectroscopy in materials science: A user-oriented guide* (Vol. 49). Springer Science & Business Media. https://books.google.com/books?hl=en&lr=&id=t_AvLetz5-YC&oi=fnd&pg=PR3&dq=Hofmann,+S.+(2013).+Auger-+and+X-ray+Photoelectron+Spectroscopy+in+Materials+Science:+A+User-Oriented+Guide.+Springer.&ots=F3xF0qZUXD&sig=oK3BuSwX-jXdZzI6wo_Nr1N09gw
12. Iravani, S. (2011). Green synthesis of metal nanoparticles using plants. *Green Chemistry*, *13*(10), 2638–2650.

IJAMSR

International Journal of Advanced Multidisciplinary Scientific Research (IJAMSR) ISSN:2581-4281

13. Jagpreet Singh, J. S., Tanushree Dutta, T. D., Kim KiHyun, K. K., Mohit Rawat, M. R., Pallabi Samddar, P. S., & Pawan Kumar, P. K. (2018). *'Green'synthesis of metals and their oxide nanoparticles: Applications for environmental remediation.* https://www.cabidigitallibrary.org/doi/full/10.5555/20203072057
14. Laurent, S., Forge, D., Port, M., Roch, A., Robic, C., Vander Elst, L., & Muller, R. N. (2008). Magnetic Iron Oxide Nanoparticles: Synthesis, Stabilization, Vectorization, Physicochemical Characterizations, and Biological Applications. *Chemical Reviews*, *108*(6), 2064–2110. https://doi.org/10.1021/cr068445e
15. Lodhia, J., Mandarano, G., Ferris, N. J., Eu, P., & Cowell, S. F. (2010). Development and use of iron oxide nanoparticles (Part 1): Synthesis of iron oxide nanoparticles for MRI. *Biomedical Imaging and Intervention Journal*, *6*(2), e12.
16. Mahmoudi, M., Hofmann, H., Rothen-Rutishauser, B., & Petri-Fink, A. (2012). Assessing the In Vitro and In Vivo Toxicity of Superparamagnetic Iron Oxide Nanoparticles. *Chemical Reviews*, *112*(4), 2323–2338. https://doi.org/10.1021/cr2002596
17. Pankhurst, Q. A., Connolly, J., Jones, S. K., & Dobson, J. J. J. (2003). Applications of magnetic nanoparticles in biomedicine. *Journal of Physics D: Applied Physics*, *36*(13), R167.
18. Priyanka, M., Karthikeyan, M., & Chand, M. S. R. (2020). Development of mix proportions of geopolymer lightweight aggregate concrete with LECA. *Materials Today: Proceedings*, *27*, 958–962.
19. Sahoo, S. K., Parveen, S., & Panda, J. J. (2017). The present and future of nanotechnology in human health care. *Nanomedicine in Cancer*, 775–806.
20. Singh, J., Dutta, T., Kim, K.-H., Rawat, M., Samddar, P., & Kumar, P. (2018). 'Green' synthesis of metals and their oxide nanoparticles: Applications for environmental remediation. *Journal of Nanobiotechnology*, *16*(1), 84. https://doi.org/10.1186/s12951-018-0408-4
21. Wáng, Y. X. J., & Idée, J.-M. (2017a). A comprehensive literatures update of clinical researches of superparamagnetic resonance iron oxide nanoparticles for magnetic resonance imaging. *Quantitative Imaging in Medicine and Surgery*, *7*(1), 88.
22. Wáng, Y. X. J., & Idée, J.-M. (2017b). Erratum to a comprehensive literatures update of clinical researches of superparamagnetic resonance iron oxide nanoparticles for magnetic resonance imaging. *Quantitative Imaging in Medicine and Surgery*, *7*(3), 383.